



The diode-pumped continuous-wave Raman laser : classical, Quantum, and thermo-optic fundamentals
by Peter Aaron Roos

A thesis submitted in partial fulfillment of the requirements of the degree Masters of Science
Montana State University

© Copyright by Peter Aaron Roos (2002)

Abstract:

This thesis describes the creation and development of far-off-resonance diode-pumped cw Raman lasers using high-finesse cavity enhancement from both theoretical and experimental standpoints. Comprehensive theoretical models are developed for the cw Raman system in the classical and quantum mechanical domains. The classical treatments include two separate derivations of the time-dependent cw Raman equations (one as an appendix), derivations of the analytical steady-state threshold power, impedance-matching power, all emitted powers, and conversion efficiency, as well as the system optimization with respect to every parameter available, and a useful frequency tuning picture (as an appendix). An entire chapter is devoted to the classical treatment of thermo-optic effects in this laser system including mode pulling and thermal lensing.

The quantum mechanical treatment uses the Heisenberg/Langevin approach to derive the Stokes output noise spectra analytically for this system. Subsequent analysis reveals the possibility of approaching perfect photon statistics transfer from the pump to the Stokes and generating nonclassical photon number statistics. An interesting and useful connection to the nondegenerate optical parametric oscillator is uncovered. The quantum mechanical approach is also used to show that a similar system can generate efficient cw anti-Stokes emission.

The process of constructing these laser systems and the subsequent measured behavior comprise the experimental component of this thesis. Diode laser frequency locking for this system is treated thoroughly as an exercise in precision frequency stabilization and control theory. The optimal designs of the diode laser pump source, the high-finesse Raman laser cavity, and the electronic servo are discussed. The use of injection locking and passive optical frequency stabilization are also addressed.

Using these construction and locking techniques, the results from diode-pumped cw Raman laser experiments in diatomic hydrogen gas are provided and are shown to compare favorably with the theoretical predictions. The results include steady-state data obtained from the first diode-pumped cw Raman laser, the first high efficiency cw Raman laser, a cw Raman laser pumped by an injection-locked diode laser, and the first cw Raman ring laser. Data confirming the effects of thermal mode pulling and lensing are also provided.

**THE DIODE-PUMPED CONTINUOUS-WAVE RAMAN LASER: CLASSICAL,
QUANTUM, AND THERMO-OPTIC FUNDIMENTALS**

by

Peter Aaron Roos

**A thesis submitted in partial fulfillment
of the requirements of the degree
Masters of Science**

**MONTANA STATE UNIVERSITY
Bozeman, Montana**

October 2002

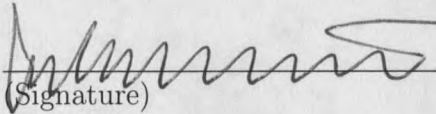
D378
R676

APPROVAL

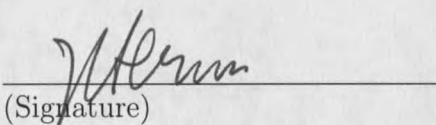
of a dissertation submitted by

Peter Aaron Roos

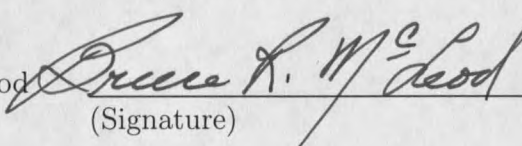
This dissertation has been read by each member of the dissertation committee and has been found to be satisfactory regarding content, English usage, format, citations, bibliographic style, and consistency, and is ready for submission to the College of Graduate Studies

John L. Carlsten  10-14-02
(Signature) Date

Approved for the Department of Physics

John C. Hermanson  10-14-02
(Signature) Date

Approved for the College of Graduate Studies

Bruce R. McLeod  10-16-02
(Signature) Date

STATEMENT OF PERMISSION TO USE

In presenting this dissertation in partial fulfillment of the requirements for a doctoral degree at Montana State University, I agree that the Library shall make it available to borrowers under rules of the Library. I further agree that copying of this dissertation is allowable only for scholarly purposes, consistent with "fair use" as prescribed in the U. S. Copyright Law. Requests for extensive copying or reproduction of this dissertation should be referred to Bell & Howell Information and Learning, 300 North Zeeb Road, Ann Arbor, Michigan 48106; to whom I have granted "the exclusive right to reproduce and distribute my dissertation in and from microform along with the non-exclusive right to reproduce and distribute my abstract in any format in whole or in part."

Signature



Date

10/14/02

ACKNOWLEDGEMENTS

I must first thank my partner, Jennifer, my sister, Bonnie, and my parents, Kathy and Roger for their unwavering love and encouragement throughout my graduate work and especially while I was writing this thesis. They have been incredibly supportive during one of the most difficult, but rewarding times of my life.

I also thank Sally O'Neill for her critical guidance and assistance during the Fulbright application process. As a direct result of her efforts, I can also thank Tim Ralph, Andrew White, Rodney Polkinghorne, Michael Nielsen, Joe Altepeter, and all the folks at the University of Queensland physics for helping to make my experience in Australia one of the best of my life. This experience (the guidance of Tim and Andrew in particular) also led to the findings presented in Chapter 3.

I am grateful to Norm in the shop for teaching me basically everything I know about machining, as well as Margaret, Jeannie, Rose and Jeremy in the office for their assistance with my day-to-day activities. These people have kept me and the whole department running smoothly.

Thanks to Tom and Pete for their friendship and advice with frequency locking. These are two very talented physicists who have thankfully not lost their appreciation nor their devotion to the wonderful outdoors.

Thanks go to Sytil, Tina, Brian, and Jennifer for making the past year so enjoyable in the lab. Our lunchtime discussions will be sorely missed. Furthermore, Sytil was kind enough to edit this entire thesis. But more importantly, she played a significant role in the findings of Chapter 5. I had a wonderful time working with her this summer.

I thank Monty for his friendship and for keeping me sane with daily climbing or bouldering excursions. We shared many good times and laughs together. We've never discussed physics with each other, and I'm sure we never will. True lifelong dirtbag friends like Monty are impossible to replace.

I am also thankful to Randy for his friendship, climbing, and physics discussions during our graduate years. I greatly admire Randy's ability to balance his roles as a caring father and husband with his amazing skills and productivity as a physicist.

I give special thanks to my predecessor Jay not only for his true friendship, but also for giving me such an incredible head start in the field of cw Raman lasers. Jay has an extraordinary gift as an experimentalist in the lab. He is the most natural person in that environment that I've ever seen. I can only hope that some of his talent rubbed off on me. I'll always enjoy working with Jay in the lab, not to mention shooting pool and drinking beer with him at the bars. He's an all-round friend.

I am grateful to Josh Bienfang for some of the most stimulating physics discussions that I've had as a graduate student. Josh has an ability blend rock-solid mathematics and theory with superb experimental skills to yield unparalleled understandings of

physics. Of my contemporaries, he is the most talented all-round physicist that I know of (even though we have yet to actually meet in person). Josh played a *major* role in the development of Appendix B and Chapter 4. I've learned a great deal from our interactions and I truly hope they continue in the future.

I also thank Lei for his wonderful companionship and friendship during our graduate work. We shared both lab space and living space while writing our theses. During my year in Australia, I realized how valuable our day-to-day discussions on physics really were. Those interactions will be missed in the future. Almost every experiment in Chapter 6 was conducted with Lei. His dedication and attention to detail make him a superb physicist. His thoughtfulness and sense of humor make him an genuine friend.

Last, but definitely not least, I thank my advisor, John. This guy has undoubtedly had the single most profound influence on my development as a physicist. But the wonderful thing about John is that his teachings transcend physics. He has dramatically influenced my thoughts and philosophies about life as well. John magically combines knowledge, experience, skill, and compassion like no one I've ever met. He has provided guidance beyond anything I could have asked for. He will remain a cherished colleague and friend throughout my life.

TABLE OF CONTENTS

LIST OF TABLES	x
LIST OF FIGURES	xi
1. INTRODUCTION	1
Stimulated Raman Scattering: A Brief Review	1
Near-resonance SRS	4
Far-off-resonance SRS	4
Cavity-Enhanced CW Raman Lasers	7
Diode Pumping and Applications	10
Ring-Cavity Geometry	12
Overview of this Thesis	14
2. CLASSICAL THEORY	18
Previous Work	20
Raman Power Rate Equations	21
Raman Gain Coefficient	24
Steady-State Powers	27
Threshold Power	28
Emitted Powers	29
Impedance-Matching Power	32
Raman Laser Optimization	34
Optimum Pump Rate	35
Optimum Input and Output Coupling	36
Optimum Detuning	39
Optimum Cavity Geometry	41
Chapter Summary	44
3. QUANTUM THEORY	45
Previous Work	47
Hamiltonian	49
Free Energy	51
Reversible Interaction Energy	51
Irreversible Interaction Energy	52
Bath Energy	54
Multiplications and Commutations	54
Quantum Langevin Equations	55
Heisenberg Equation of Motion	56

Rotating Coordinate Transformations	59
Field Equations	61
Two-Photon Coherence Equation	61
Single-Photon Coherence Equations	62
Population Equations	66
Simplifications Based on Large Detunings	67
Semiclassical Analysis	71
Simplified Population Equations	72
Simplified Field Equations	76
Steady-State Behavior	76
Spatial Considerations	79
Connection to the NDOPO	79
Operator Correlation Functions	80
System Comparison	82
Alternative Forms of the Hamiltonian	85
Output Intensity Noise Spectra	88
Amplitude/Phase Decoupling	90
Linearization	91
Input/Output Formalism	93
Intensity Noise	94
Stokes Intensity Noise Analysis	98
Chapter Summary	104
4. THERMO-OPTIC THEORY	107
Previous Work	109
Thermal Refractive Index Profile	111
Heat Deposition Profile	111
On-Axis Thermal Power Density	114
Near-Axis Refractive Index Profile	115
Thermal Mode Pulling	119
Practical Considerations	120
Thermal Lensing	121
Cavity with Quadratic Duct	122
Simplified Confocal Parameter	124
Modified Steady-State Behavior	126
Chapter Summary	130
5. FREQUENCY LOCKING	132
Previous Work	135
Experimental Layout	138
ECDL Pump Laser Design	141
Littman-Metcalf Configuration	144
Littrow Configuration	146

Assessing the Pump Laser Frequency Noise	149
Pump Laser Transfer Function	154
Pump Laser Subsystem.....	157
Raman Laser Cavity Design.....	158
Linear Cavity	160
Ring Cavity	162
Raman Cavity Transfer Function	164
Raman Cavity Subsystem	165
Electronic Servo Design.....	168
Generating the Error Signal.....	168
Identifying the Loop Response.....	170
Designing the Servo Electronics	172
Slow Frequency Corrections.....	177
Closing the Feedback Loop.....	178
Injection Locking	182
Passive Optical Stabilization	187
Chapter Summary.....	191
6. EXPERIMENTAL RESULTS.....	193
Previous Work.....	194
Diode-Pumped Raman Lasing	195
High-Efficiency Raman Lasing	202
Injection-Locked Raman Lasing.....	207
Raman Laser Thermal Mode Pulling	212
Raman Laser Thermal Lensing.....	221
Unidirectional Raman Ring Lasing	226
Chapter Summary.....	229
7. SUMMARY	231
APPENDIX A – LASER-CAVITY FIELD EQUATION	236
APPENDIX B – RAMAN LASER EQUATIONS: LAMB APPROACH	240
APPENDIX C – BOW-TIE CAVITY EIGENMODE.....	256
APPENDIX D – FREQUENCY TUNING DESCRIPTION.....	266
APPENDIX E – PUMP LANGEVIN EQUATION	272
APPENDIX F – 1-3 COHERENCE LANGEVIN EQUATION	276
APPENDIX G – ANTI-STOKES THEORY.....	280
APPENDIX H – SIMPLIFIED PUMP EQUATION	297
APPENDIX I – SIMPLIFIED S_{12} EQUATION	301
APPENDIX J – COHERENT STATE POWER SPECTRAL DENSITY ...	305
APPENDIX K – DIFFUSED WAIST	309
APPENDIX L – TEMPERATURE DISTRIBUTION	311
APPENDIX M – SERVO CIRCUIT.....	314

LIST OF TABLES

Table	Page
1. Definitions of single-photon detunings.	65
2. Parameters used for simplifying the quantum Langevin equations.	67

LIST OF FIGURES

Figure	Page
1. Simple picture of the stimulated Raman process. An incident pump photon is converted to a lower energy (longer wavelength) stimulated Stokes photon and the leftover energy remains in the Raman medium. .	1
2. Frequency downconversion using the stimulated Raman process. Because this involves phase insensitive amplification of the Stokes light, the system shown is often called a Raman laser. The laser action is initiated by spontaneously emitted Stokes photons.....	2
3. Simplified energy level diagrams for the (a) near-resonance and (b) far-off-resonance Raman processes. The large detuning (Δ) causes the gain for the far-off-resonance process to be much lower than for the near-resonance process.	3
4. Diagram depicting the Stokes laser threshold for three different enhancement techniques. The diagram emphasizes the usefulness of high-finesse cavity (HFC) enhancement of both the pump and the Stokes fields. Specifically, the far-off-resonance Raman transition can be enhanced by nearly nine orders of magnitude.	8
5. Simplified block diagram of the essential cw Raman laser elements. The high-finesse cavity (HFC) is filled with diatomic hydrogen gas.....	9
6. Diagram showing the spectral coverage of currently available room temperature diode lasers and their Raman-shifted outputs in methane and diatomic hydrogen gas. This figure was originally developed by John Carlsten.	11
7. Diagram showing the incident, reflected, and circulating beams of a linear cavity and a bow-tie ring cavity. The reflected field does not return to the source for the ring geometry.	13
8. Illustration showing the ring-cavity geometry with the relevant fields. The laser medium occupies the entire intracavity volume.....	22

9. (a) Emitted and (b) reflected powers from the cw Raman laser cavity versus pump rate. The transmitted pump power is clamped above threshold ($r_p = 1$), while the emitted Stokes power exhibits a square-root dependence on the pump rate. By increasing the input coupler transmissivity ($T_{p,0}$) relative to the other intracavity losses at the pump wavelength ($A_{p,gen}$) impedance matching can occur above threshold, but not greater than four times threshold. The parameters used to generate these curves are: $P_1 = 24\text{kW}$, $R_{p,0} = R_{s,0}^3 = 0.9998$, $T_{p,0} = 200\text{ppm}$, and $R_{p,1} = R_{s,1}^3 = 0.9998$ 31
10. Photon conversion efficiency versus the pump rate relative to the curve A threshold. The mirror transmissivities for curve A are chosen such that the threshold occurs at 1/4 of the maximum available pump power. The transmissivities for curve B are chosen according to Eqs. (2.36) and (2.37) and maximize the conversion efficiency for the available pump power. 38
11. (a) Stokes output power versus detuning from the two-photon Raman transition line center (Δ_{12}) for several different pump rates. (b) Optimum detuning (horizontal axis) versus pump rate (vertical axis). .. 41
12. Inverse cosecant function (which is proportional to the focused gain) as a function of curvature-to-length ratio (R/L). The figure suggests that the concentric cavity geometry is optimal, but practical concerns favor other geometries. 43
13. To-scale energy level diagram for the diatomic hydrogen molecule showing the pertinent levels and the far-off-resonance fields. The arrows below the energy levels represent counter-rotating terms that must be included due to the large single-photon detunings (Δ 's). 50
14. To-scale energy level diagram for the diatomic hydrogen molecule after simplifications based on large single-photon detunings. 70
15. Plot showing the growth of the level two population as a function of the scaled time $\bar{\gamma}_{21}t$, where $\bar{\gamma}_{21}$ is the population decay rate of level two. The population approaches its steady-state value of $\Gamma_{12}/\bar{\gamma}_{21}$ with a rise time of $\bar{\gamma}_{21}^{-1}$, where Γ_{12} is the two-photon excitation rate to level two. 75

16. (a) Linear and (b) log-log plots of the Stokes intensity noise relative to the SQL as a function of pump rate for frequencies well below the cavity linewidths. Curves for several different values of the input pump intensity noise $[V_p^{\text{in}}(\omega)]$ are shown. The system exhibits perfect photon statistics transfer from pump to Stokes at four times threshold and the intensity noise approaches 50% below the SQL in the limit of large pump rate. 100
17. Stokes intensity noise relative to the SQL as a function of normalized Fourier frequency for several different ratios of the cavity decay rates (κ_s/κ_p) and for a pump rate of (a) 4 times threshold and (b) 25 times threshold. The product $\kappa_s \times \kappa_p$ is held constant for all curves so that they correspond to the same threshold. Decreasing the cavity decay rate of the Stokes relative to that of the pump suppresses relaxation oscillations. Increasing the pump rate from (a) $r_p = 4$ to (b) $r_p = 25$ in produces broadband suppression of the intensity noise and pushes the relaxation oscillations to slightly higher frequencies..... 102
18. Stokes intensity noise relative to the SQL as a function of normalized Fourier frequency for several different pump rates, equal cavity decay rates ($\kappa_s = \kappa_p$) and for an input pump noise of (a) $V_p^{\text{in}}(\omega) = 10$ and (b) $V_p^{\text{in}}(\omega) = 1$ (coherent state). Again, the product $\kappa_s \times \kappa_p$ is held constant for all curves. The relaxation oscillations are diminished and pushed to higher frequencies as the pump rate is increased..... 103
19. Plot showing the the radial pump power, Stokes power, population, and thermal profiles within the cavity for comparison of the relative waists. All of the Gaussians are normalized to a peak of unity. 113
20. Plot showing the normalized refractive index distribution as a function of the radial distance from the beam axis relative to the pump field waist. The quadratic and tenth-order approximations to the exact fit are also shown. 118
21. Plot showing transmitted pump powers as functions of the pump rate. The solid line represents the predicted behavior when thermal effects are ignored. The dotted line shows the behavior including thermal effects for the ring cavity and the dashed line shows the same for the linear cavity..... 128
22. Plot showing the output Stokes pump power and the photon conversion efficiency as functions of the pump rate. 129

23. Scale of possible diode laser stabilization schemes. Most feedback configurations, including ECDL locking, use some passive and some active feedback for frequency noise reduction. 135
24. Flexible and useful experimental layout for the diode-pumped Raman laser system. The layout is divided into three optical subsystems and an electronic servo. The use of optical fibers facilitates beam alignments and adjustments. 139
25. Simple diagram showing the Littman-Metcalf and Littrow configuration external-cavity diode lasers (ECDLs). There are advantages and drawbacks for each configuration. 142
26. (a) Front and (b) back images of the Littman-style ECDL designed and constructed by Gregg Switzer. 145
27. (a) Back and (b) front images of the Littrow-style ECDL designed to produce a more robust lock to the high-finesse Raman laser cavity. 147
28. Setup used to measure the frequency noise spectral density of the ECDLs. The Fabry-Perot (FP) length is adjusted via low bandwidth feedback and a PZT to ensure that the laser remains parked on the side of the FP transmission peak. 151
29. Data showing the frequency noise spectral density as a function of Fourier frequency for the Littman (trace A) and Littrow (trace B) ECDL configurations. 153
30. The curves labeled A show the measured magnitude and phase of the diode laser modulation transfer function. The curves labeled B show the predicted behavior assuming a single pole at 400kHz. The excessive phase lag exhibited in the diode laser's modulation response limits the servo bandwidth. 156
31. Setup for the pump laser subsystem. The output from this subsystem can either go to the injection locking subsystem for amplification or directly to the Raman cavity subsystem for conversion to Stokes. 157
32. Schematic cross-section of the linear cavity design. The schematic is not exactly to scale and does not show all the components of the apparatus. 160
33. Image of the linear cavity used for cw Raman conversion. 162

34. Schematic cross-section of the bow-tie style ring cavity design. The schematic is not exactly to scale and does not show all the components of the apparatus.....	163
35. Image of the ring cavity used for Raman conversion.	164
36. Theoretical transfer function of the high-finesse Raman cavity. This response need not be measured because it is very predictable.	165
37. Setup for the Raman cavity subsystem. The input pump light can come from either the pump laser subsystem or the injection locking subsystem.....	167
38. Composite transfer functions (magnitude and phase) of the diode and cavity frequency responses. The purpose of the servo is to compensate for the excess phase lag introduced by these two loop elements.	171
39. The curves in part A show the measured response of just an integrator with a zero. Part B shows the that of a phase lead compensator. Part C shows the composite measured response of the servo.	174
40. The closed-loop phase response including the diode, the cavity, and the servo. The servo preserves the phase past 1MHz.	175
41. The closed loop magnitude response including the diode, the cavity, and the servo.	176
42. Data showing the frequency noise spectral density as a function of Fourier frequency for (trace A) a typical free-running diode laser, (trace B) a Littrow ECDL, and (trace C) the same Littrow ECDL that is electronically stabilized to the HFC.	181
43. Setup for the injection locking subsystem.	184
44. Traces A and B in the figure show the spectral output from a free-running slave laser with no injected signal, while trace C shows the output of the same laser with an injected signal.	186
45. Possible setup for the passively-locked cw Raman laser.	189

46. Passively locked experimental setup used to demonstrate the first diode-pumped cw Raman laser. LD = laser diode, APP = anamorphic prism pair, GP = Glan polarizer, FR = Faraday rotator, $\lambda/2$ = half-wave plate, PBS = polarizing beam splitter, EOM = electrooptic modulator, BS = beam splitter, MML = mode matching lenses, M = mirror, PBP = Pellin-Broca prism, and HFC = high finesse cavity. Mirror M1 is reflective coated only for the pump wavelength..... 197
47. HFC output powers for the transmitted pump at 790nm (squares) and Stokes at 1178nm (circles) as functions of input pump power. The solid lines represent theoretical models developed in either Chapter 2 or 3. The Stokes laser threshold is observed at 240 ± 19 mW. 199
48. Photon conversion efficiency from the pump to the Stokes beam as a function of input optical power. The solid line represents theoretical predictions from Chapter 2. The efficiency rises throughout the pump power region studied with a peak value of 15%. 201
49. Passive locking experimental setup used to demonstrate the first high-efficiency cw Raman laser. See the caption of Fig. 46 for symbol definitions..... 203
50. Plot showing the output Stokes power and photon conversion efficiency from the impedance-matched Raman high-finesse cavity as functions of the coupled pump power. This system exhibited ~ 14 mW of output Stokes power, $\sim 61\%$ photon conversion efficiency, and it provided the first indication that the basic Raman laser theory was insufficient for high-power systems..... 205
51. Reflected and transmitted pump powers from the impedance-matched Raman laser cavity as functions of the coupled pump power. The behavior of this system provided the first clear indication that the basic Raman laser theory was insufficient for high-power systems. 206
52. Injection locking experimental setup. The use of an optical fiber between the ECDL master and the free-running diode laser (FRDL) slave enables automatic alignment of the injected beam, as discussed in Chapter 5. See the caption of Fig. 46 for symbol definitions. 208
53. Plot showing the output Stokes power (circles), transmitted pump power (diamonds), and photon conversion efficiency (squares) as functions of the coupled input pump power. The injection locking technique enabled a pump rate of 90 times threshold to be achieved..... 211

54. Experimental setup used to measure the intensity-dependent thermal mode pulling. Thermally-induced shifts in the Raman laser cavity length (HFC) were manifest as voltage applied to the PZT elements. ... 214
55. Plot showing the measured PZT voltage versus the pump optical power. A clear behavioral change is observed at the Stokes laser threshold ($840\mu\text{W}$). 215
56. Experimental data showing the mode pulling as a function of the generated Stokes optical power. 217
57. Experimental data showing the subtle mode pulling below threshold as a function of the coupled pump optical power. 219
58. Plot showing the measured transmitted pump power and the Raman laser cavity length while scanning the cavity and *not* locking. 220
59. Transmitted (circles) and reflected (squares) pump powers from a high-power Raman system. The thermo-optic theory significantly improves the agreement with the measured data. 222
60. Plot showing the output Stokes power (circles) and photon conversion efficiency (squares) as functions of the incident pump power. The reduction in the Stokes output is due to the thermal lensing. 223
61. Plot showing the relative far-field beam waist as a function of the incident pump power. The squares are were taken when no Stokes was generated (detuned from the Raman line center), whereas the circles were taken with Stokes. 225
62. Data showing stable operation in the forward direction of the first cw Raman ring laser. The dashed lines show the basic theory and the solid lines show the theory when the thermo-optic modifications are included. 228
63. Frequency tuning picture for a doubly-resonant cw Raman laser. The picture is not to scale. Part (a) shows the HFC (high-finesse cavity) modes for a round-trip cavity length of p , whereas part (b) shows the modes for a longer round-trip cavity length of p' . The picture illustrates how changing the cavity length will tune the Stokes cavity mode across the Raman gain profile by an amount Δ_{12} 268

64. To-scale energy level diagram showing (a) the pertinent atomic levels, fields (α 's) and single-photon detunings (Δ 's), and (b) the energy flow for the overall anti-Stokes generation process. 283
65. Photon conversion efficiencies for (a) the Stokes and (b) the anti-Stokes fields as functions of the pump rate. Curves are given for several different values of the relative gain parameter x , and for idealized experimental conditions. 290
66. Plots showing (a) the normalized laser threshold and (b) the photon conversion efficiency as functions of the relative gain parameter x . The solid curves represent idealized conditions, the dotted curves labeled B include imperfect spatial overlap and phase matching, and the dotted curves labeled C additionally include mirror losses. 292
67. Schematic illustrating how dispersion can inhibit the generation of anti-Stokes. When no dispersion exists (a), the anti-Stokes is automatically generated on a cavity resonance. However, due to dispersion in the Raman medium, the anti-Stokes frequency does not automatically match that of a cavity resonance. 294
68. Servo circuit for fast feedback to the diode laser injection current. 315

ABSTRACT

This thesis describes the creation and development of far-off-resonance diode-pumped cw Raman lasers using high-finesse cavity enhancement from both theoretical and experimental standpoints. Comprehensive theoretical models are developed for the cw Raman system in the classical and quantum mechanical domains. The classical treatments include two separate derivations of the time-dependent cw Raman equations (one as an appendix), derivations of the analytical steady-state threshold power, impedance-matching power, all emitted powers, and conversion efficiency, as well as the system optimization with respect to every parameter available, and a useful frequency tuning picture (as an appendix). An entire chapter is devoted to the classical treatment of thermo-optic effects in this laser system including mode pulling and thermal lensing.

The quantum mechanical treatment uses the Heisenberg/Langevin approach to derive the Stokes output noise spectra analytically for this system. Subsequent analysis reveals the possibility of approaching perfect photon statistics transfer from the pump to the Stokes and generating nonclassical photon number statistics. An interesting and useful connection to the nondegenerate optical parametric oscillator is uncovered. The quantum mechanical approach is also used to show that a similar system can generate efficient cw anti-Stokes emission.

The process of constructing these laser systems and the subsequent measured behavior comprise the experimental component of this thesis. Diode laser frequency locking for this system is treated thoroughly as an exercise in precision frequency stabilization and control theory. The optimal designs of the diode laser pump source, the high-finesse Raman laser cavity, and the electronic servo are discussed. The use of injection locking and passive optical frequency stabilization are also addressed.

Using these construction and locking techniques, the results from diode-pumped cw Raman laser experiments in diatomic hydrogen gas are provided and are shown to compare favorably with the theoretical predictions. The results include steady-state data obtained from the first diode-pumped cw Raman laser, the first high efficiency cw Raman laser, a cw Raman laser pumped by an injection-locked diode laser, and the first cw Raman ring laser. Data confirming the effects of thermal mode pulling and lensing are also provided.

CHAPTER 1

INTRODUCTION

Stimulated Raman Scattering: A Brief Review

The stimulated Raman effect was discovered in 1962 [1], shortly after the advent of the laser. One can view this two-photon process most simply as an exchange of “pump” photons for lower energy “Stokes” photons through a stimulated interaction with a Raman-active medium as illustrated in Fig. 1. The energy difference between the incident pump and stimulated Stokes photons resides within the Raman medium after the interaction, often in the form of a molecular vibration.

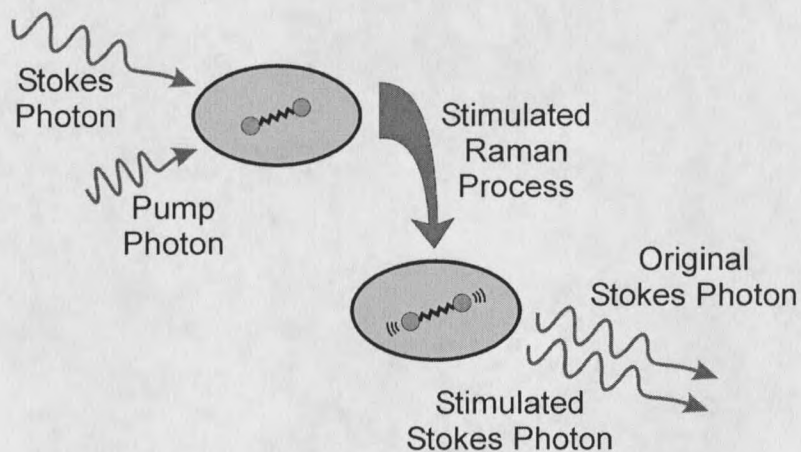


Figure 1. Simple picture of the stimulated Raman process. An incident pump photon is converted to a lower energy (longer wavelength) stimulated Stokes photon and the leftover energy remains in the Raman medium.

This process can result in exponential growth (amplification) of input Stokes light at the expense of the input pump light. But even when there is no input Stokes, the process can be initiated by spontaneous emission alone. In other words, by simply directing an intense pump laser through a Raman medium, some of the pump light will be converted to the Stokes frequency, as shown in Fig. 2. Stimulated Raman scattering (SRS) therefore provides, among other things, a valuable method of downshifting the frequency of laser light. However, this stimulated process differs from parametric conversion processes in that the phase of the generated Stokes light doesn't directly depend on that of the pump. Due to this phase-insensitive amplification, the system shown in Fig. 2 is often considered to be an optically-pumped laser; more specifically, a Raman laser.

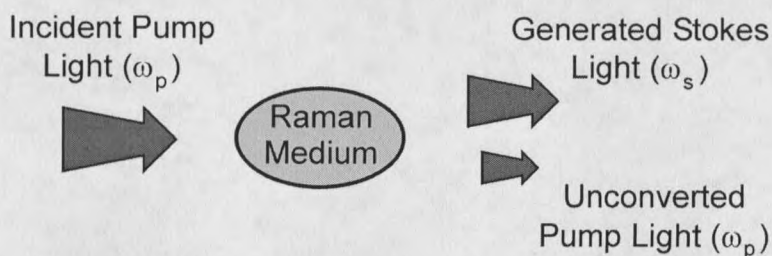


Figure 2. Frequency downconversion using the stimulated Raman process. Because this involves phase insensitive amplification of the Stokes light, the system shown is often called a Raman laser. The laser action is initiated by spontaneously emitted Stokes photons.

